Laser-Assisted Floating Zone Growth of BaFe₂S₃ Large-Sized Ferromagnetic-Impurity-Free Single Crystals

Maria Lourdes Amigó [1,*] , **Andrey Maljuk** [1] , **Kaustuv Manna** [2,3] , **Quirin Stahl** [4] , **Claudia Felser** [2] , **Christian Hess** [1,†] , **Anja U.B. Wolter** [1] , **Jochen Geck** [4,5] , **Silvia Seiro** [1] and **Bernd Büchner** [1,4,5]

[1] Leibniz IFW Dresden, Helmholtzstr. 20, 01069 Dresden, Germany; a.malyuk@ifw-dresden.de (A.M.); c.hess@uni-wuppertal.de (C.H.); a.wolter@ifw-dresden.de (A.U.B.W.); s.seiro@ifw-dresden.de (S.S.); B.Buechner@ifw-dresden.de (B.B.)

[2] Max-Planck-Institut für Chemische Physik Fester Stoffe, 01187 Dresden, Germany; kaustuvmanna@gmail.com (K.M.); Claudia.Felser@cpfs.mpg.de (C.F.)

[3] Department of Physics, Indian Institute of Technology Delhi, Hauz Khas, New Delhi 110016, India

[4] Institut für Festkörper- und Materialphysik, Technische Universität Dresden, 01069 Dresden, Germany; quirin.stahl@tu-dresden.de (Q.S.); jochen.geck@tu-dresden.de (J.G.)

[5] Würzburg-Dresden Cluster of Excellence ct.qmat, Technische Universität Dresden, 01062 Dresden, Germany

* Correspondence: m.l.amigo@ifw-dresden.de

† Current address: Fakultät für Mathematik und Naturwissenschaften, Bergische Universität Wuppertal, 42097 Wuppertal, Germany.

Abstract: The quasi-one-dimensional antiferromagnetic insulator BaFe₂S₃ becomes superconducting under a hydrostatic pressure of ∼10 GPa. Single crystals of this compound are usually obtained by melting and further slow cooling of BaS or Ba, Fe, and S, and are small and needle-shaped (few mm long and 50–200 μm wide). A notable sample dependence on the antiferromagnetic transition temperature, transport behavior, and presence of superconductivity has been reported. In this work, we introduce a novel approach for the growth of high-quality single crystals of BaFe₂S₃ based on a laser-assisted floating zone method that yields large samples free of ferromagnetic impurities. We present the characterization of these crystals and the comparison with samples obtained using the procedure reported in the literature.

Keywords: iron-based superconductor; BaFe₂S₃; laser-assisted floating zone technique; single crystal

1. Introduction

Since the discovery of superconductivity in LaO$_{1-x}$F$_x$FeAs in 2008 [1], a great effort was devoted to the study of iron-based superconductors [2–4]. While most of the materials in this class share a layered crystalline structure [5], the finding of superconductivity in the quasi-one-dimensional iron chalcogenides BaFe₂S₃ [6,7] and BaFe₂Se₃ [8] represented an interesting surprise. The building blocks of these compounds are two-leg ladders of edge-sharing Fe(S,Se)₄ tetrahedra, as shown in Figure 1 for BaFe₂S₃, that contrast with the planes of FeAs₄ or FeSe₄ tetrahedra common to other members of the family. BaFe₂S₃ and BaFe₂Se₃ also differ from other iron-based superconductors in that they are antiferromagnetic insulators at ambient pressure and superconductivity only emerges under hydrostatic pressure [6–9]. These unique characteristics make them intensively studied both theoretically and experimentally [10–13].

BaFe₂S₃ presents a stripe-type antiferromagnetic order below $T_N \sim 120$ K [6]. Under hydrostatic pressure, T_N increases up to 185 K for 7.5 GPa and then undergoes a sudden drop near the insulator-to-metal transition [14]. The superconducting state emerges at $P \sim 10$ GPa, reaching a maximum $T_c \sim 24$ K [7]. However, the value of the Néel temperature and the presence of superconductivity seem to depend on specific features of the growth procedure [6,15–17]. Starting from a stoichiometric ratio of BaS or Ba, Fe, and S does not always lead to samples that present superconductivity under hydrostatic pressure [6,17]. The use

of a slight Fe excess in the nominal content was reported to promote the appearance of superconductivity. Moreover, samples that present superconductivity under hydrostatic pressure were reported to have higher values of T_N [6]. Another typical problem of the samples described in the literature is the existence of impurity phases that are clearly seen in magnetization loops, obscuring the intrinsic properties of $BaFe_2S_3$ [15,18]. The fact that these impurity phases exhibit a rather large magnetic response makes the accurate description of the intrinsic physical properties of $BaFe_2S_3$ a real challenge. It is also unclear how the sample purity affects the appearance of superconductivity at high pressure.
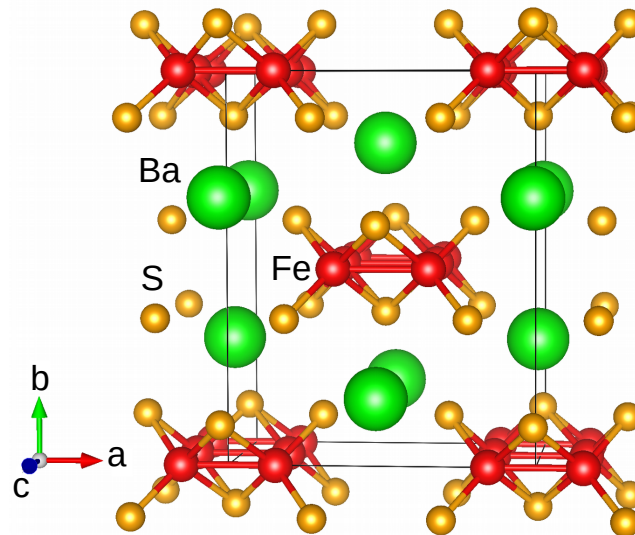

Figure 1. Crystal structure of the quasi-one-dimensional iron chalcogenide $BaFe_2S_3$.

Previously, we have reported the growth of $BaFe_2S_3$ crystals using a Bridgman-like method based on optical heating [15]. This approach allowed us to obtain samples free of ferromagnetic impurities, although tiny traces of nonmagnetic SiO_2 inclusions have been detected due to the weak reaction between the melt and the quartz crucible. It is worth mentioning that all previously reported $BaFe_2S_3$ crystals were prepared using a crucible-based technology. From this point of view, a crucible-free floating zone technique seems to be a promising choice to grow inclusion-free $BaFe_2S_3$ crystals.

In this work, we report the floating zone growth of $BaFe_2S_3$ crystals using a laser-assisted floating zone furnace. We present a characterization of the composition, the crystal structure, the magnetization, and the resistivity of the as-grown crystals and the comparison with samples grown by the standard procedure previously reported in the literature [6,15]. This characterization confirms the improvement in the quality of the crystals and the suppression of ferromagnetic impurities.

2. Materials and Methods

The precursor material was obtained following a protocol commonly used and well described in the literature [15]. BaS powder, 200 mesh (Alfa Aesar 99.7%), Fe powder, 70 mesh (Acros organics 99%), and S pieces (Alfa Aesar 99.999%) were mixed in a molar ratio 1:2.05:2 using an agate mortar under Ar atmosphere (<0.5 ppm O_2 and H_2O). The obtained mixture was placed in a glassy carbon crucible and sealed in an evacuated quartz ampule, which was heated up to 1100 °C in a vertical position in a Nabertherm chamber furnace, and slowly cooled down to 750 °C at 10 °C/h. After 2 h at 750 °C, the furnace was switched off. An ingot was formed at the crucible bottom, from which needlelike single crystals of few mm length and 50–200 μm width could be detached.

This precursor material was ground and filled into a rubber tube in a high-purity Ar atmosphere (MB 150B-G glovebox, <0.1 ppm O_2 and H_2O). The rubber tube was tightly closed to avoid exposure to air and pressurized under a hydrostatic pressure of 2500 bar.

The pressed rod with a diameter of ~0.5 cm was finally sintered at 650 °C for 20 h in a horizontal tube furnace in Ar flow of 0.5 l/min. In order to avoid any contact between the rod and the furnace, a glassy carbon boat was used. Because of the relatively low melting point of $BaFe_2S_3$, approximately 800 °C based on our preliminary DTA measurements, the as-sintered feed rod was quite porous but mechanically stable.

Initially, we tried to grow this material using a conventional four-mirror-type image furnace (CSI, Japan) equipped with 300 W halogen lamps. Prior to the growth run, the growth chamber was evacuated down to a pressure of 10^{-3} mbar and consequently filled with Ar (5N) gas. This step was repeated three times in order to avoid oxygen contamination. Nevertheless, after 1.5–2.0 h, the molten zone was completely covered by a solid layer due to the oxidation. Additionally, a strong penetration effect was observed due to the feed rod porosity. Both effects terminated the growth run in 3–4 h.

Finally, we successfully grew $BaFe_2S_3$ using a recently developed laser-assisted floating zone furnace with a magnetic sealing (CSI, Japan) operated at MPI-CPfS Dresden. The machine was equipped with five semiconductor laser diodes with a total power of 5×200 W. The wavelength of the laser light was 976 nm with a rectangular beam profile of 4×8 mm^2. The pinpoint character of laser heating makes the temperature gradient across the solid–liquid interface extremely steep [19] (over 1500 °C/cm), preventing the penetration of liquid from the molten zone into the porous feed rod. This resulted in a stable molten zone during the whole growth run (approximately 12 h). Prior to the growth, we evacuated the chamber and the gas line up to 10^{-6} mbar and filled with purified Ar gas. Using an in-built Ar purifier (SAES Pure Gas, Inc.), the levels of O_2 and H_2O in the Ar flow were decreased from ppm to ppb level. The growth was performed at 4 mm/h. The feed and seed rod were counter-rotated at 20 rpm. The applied Ar pressure was 7 bar.

The grain selection through the rod was analyzed with an optical microscope (Carl Zeiss) using polarized light.

The composition and morphology were studied with a Zeiss EVOMA15 scanning electron microscope (SEM) with AzTec software equipped with an electron microprobe analyzer for semiquantitative elemental analysis using the energy-dispersive X-ray (EDX) mode. We used BaF_2 and FeS_2 standards and performed around 50 measurements for each sample. We only took the measurements where the total weight percent (wt %) was between 95 and 105 wt % into account.

Powder X-ray diffraction measurements were carried out in briefly crushed single crystals, since prolonged grinding proved detrimental to crystallinity, inducing considerable broadening of Bragg peaks and decreasing intensity. The data were collected at ambient temperature with a STOE STADI P diffractometer equipped with a MYTHEN 2 K detector using Mo-K$_{\alpha 1}$ radiation. The structure refinement was performed using the FullProf Suite program [20]. Due to the highly textured nature of the powder, atomic positions and displacement parameters were not refined, but initially fixed to the values obtained from the literature [15]. After the single crystal X-ray diffraction analysis, the powder X-ray diffraction refinement was revisited with the values obtained for the crystals grown by the laser-assisted floating zone method. No significant change was found, indicating good convergence of the refinement.

The single crystal X-ray diffraction data were collected at ambient temperature on a Bruker-AXS KAPPA APEX II CCD diffractometer with graphite-monochromated Mo-K$_\alpha$ X-ray radiation (50 kV, 30 mA). A single crystal of $50 \times 50 \times 90$ μm^3 in size was isolated from the as-grown ingot obtained from the laser-assisted floating zone growth and glued on top of a glass capillary. The crystal-to-detector distance was 45.1 mm. The detector was positioned at $2\Theta = 30°$ and $45°$ using an ω-scan mode strategy at four different ϕ positions (0°, 90°, 180° and 270°). The Bruker APEX3 software suite [21], SAINT [22], and SADABS [23] were used to perform the data processing, the integration of the reflection intensities, and the correction of the multiscan absorption, respectively. The subsequent weighted fullmatrix least-squares refinements on F^2 were performed with SHELX-2012 [24] as implemented in the WinGx 2014.1 program suite [25]. The crystal structure was refined

with anisotropic displacement parameters for all atoms and using the lattice constants determined via Rietveld refinement of the powder pattern.

The rocking curves were measured at room temperature using a custom-made high-resolution X-ray diffraction system, providing monochromatic Mo-K$_\beta$ radiation with a divergence of 1 mrad and a beam diameter of 90 μm. The measurements were performed in transmission geometry on a small piece (approximately 200×200 μm^2 area and 100 μm thickness) of the ingot obtained from the laser-assisted floating zone growth.

X-ray Laue back-scattering was performed using a Multiwire detector, white radiation from a tungsten X-ray tube, and a collimator of 0.5 mm.

Magnetization measurements were performed in a vibrating sample superconducting quantum interference device magnetometer (SQUID-VSM) from Quantum Design. All measurements were carried out after cooling in zero field. To reduce the remanent field of the superconducting magnet to less than 2 Oe before each measurement, we applied a magnetic field of 5 T at ambient temperature and then removed it in an oscillation mode. The magnetic field was applied parallel to the needle direction of the single crystals that corresponds to the *c*-axis.

The resistivity measurements were carried out in an OXFORD cryostat using a four-probe configuration. We used gold wires and silver paste for the electric contacts. The current was applied along the *c*-axis and its value depends on the temperature. At 300 K, we used 0.4 mA decreasing linearly to 0.1 mA at 100 K, 0.01 mA at 70 K, 0.001 mA at 60 K, 0.0001 mA at 50 K, and 0.00005 mA at 40 K. Varying the current by one order of magnitude did not induce any changes in the value of the resistivity. Therefore, we can rule out Joule heating effects. Moreover, no change in the resistivity behavior was observed when using a constant current of 0.00005 mA below 150 K.

3. Results

The stable molten zone during BaFe$_2$S$_3$ growth is shown in Figure 2. Although some level of liquid penetration into the feed could be observed, it was dramatically suppressed compared to that detected in the conventional image furnace.
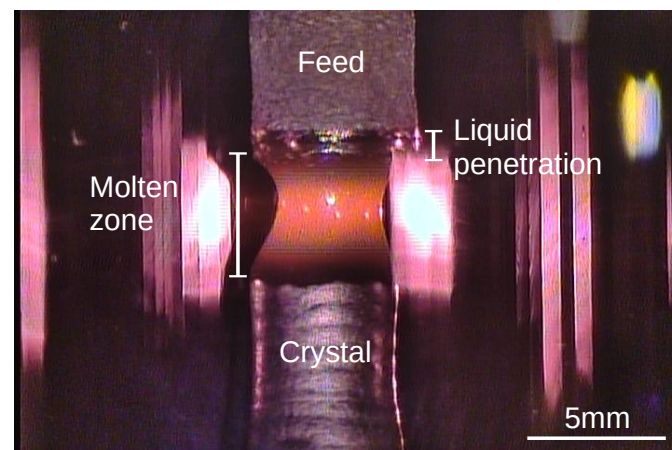

Figure 2. Crystal growth of BaFe$_2$S$_3$ in the laser floating-zone furnace.

No S evaporation was observed and the quartz tube was completely clean after the growth run. Since BaFe$_2$S$_3$ melts at a relatively low temperature of about 800 °C in Ar atmosphere, the growth was performed at low laser output power (6.7–7.0%). Nevertheless, the molten zone was extremely stable during the growth and no overspills were noticed compared to the conventional image furnace. The molten zone was not oxidized and had no solid particles on its surface in contrast to the previous experiment in a CSI image furnace. The as-grown ingot is shown in Figure 3a. Sections were cut off from the beginning and the end-portion of the as-grown ingot as indicated in Figure 3, and polished to a mirror finish. The polarized optical microscope study of these slices shows the strong grain

selection during the growth. Thus, the end-portion consists only of a few large grains (Figure 3c). In the rest of the work, the crystals obtained from this ingot will be labeled "LFZ" to differentiate them from the precursor crystals obtained by the standard growth procedure [15].
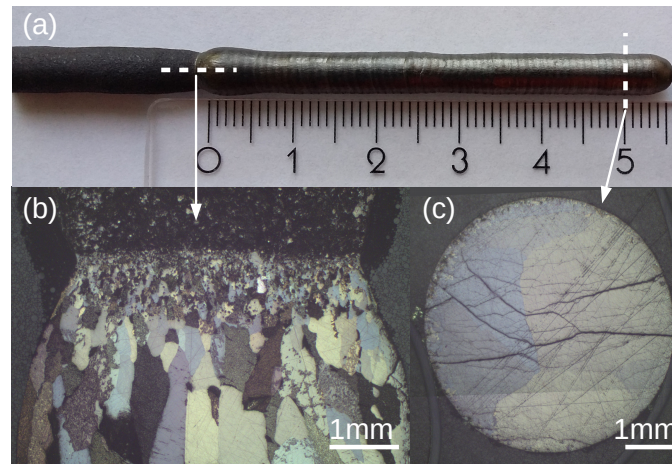

Figure 3. (**a**) As-grown ingot of BaFe$_2$S$_3$. The scale is in cm. The dotted lines indicate the cuts corresponding to (**b**) the longitudinal section of the seeding and (**c**) the cross-section of the end portion. The images in (**b**,**c**) were obtained using polarized light.

Figure 4 presents backscattered electron (BSE) images of the precursor and of the end-portion of the as-grown ingot (LFZ). While the precursor exhibits a textured surface with striations representative of the needle conglomerate, the end-portion of the ingot shows a smooth surface. The average composition in each region is in good agreement with the expected BaFe$_2$S$_3$ within the accuracy of the method [26,27], as presented in Table 1. However, the statistical dispersion of the measurements of the end-portion of the ingot is reduced by almost an order of magnitude with respect to the precursor. Though inclusions of FeS and Fe have been observed in the precursor, no impurity phases have been identified in the LFZ grown crystals.
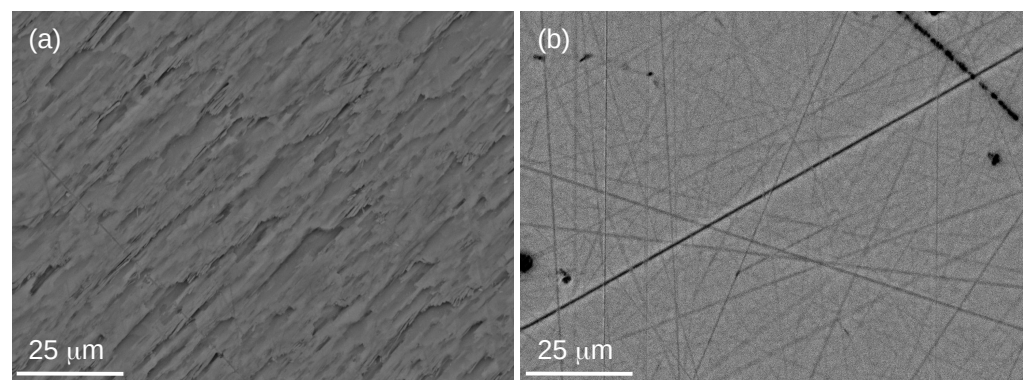

Figure 4. SEM images in the BSE-mode for (**a**) precursor and (**b**) end-part of the LFZ ingot.

All of this indicates an improvement in the quality of the samples grown with the laser-assisted floating zone furnace with respect to the standard growth procedure. This result also represents an improvement with respect to previously reported samples grown by a Bridgman-like method based on optical heating, which did not present ferromagnetic impurities but contained nonmagnetic SiO$_2$ inclusions stemming from the quartz crucible [15].

Table 1. Average composition of the precursor and the end-part of the ingot (LFZ) in at%. The standard deviation is indicated in parenthesis.

	Ba	Fe	S
Precursor	17.2(1)	32.9(3)	49.9(4)
LFZ	17.16(4)	32.79(6)	50.05(9)

Powder X-ray diffraction patterns from crushed single crystals of the precursor and LFZ samples are presented in Figure 5a. The majority of the reflections can be identified with the orthorhombic structure with a space group *Cmcm* previously reported for $BaFe_2S_3$ [6,15,28,29]. The differences in the relative intensity of the reflections between both samples can be associated with the preferred orientation in the powder due to the strong anisotropic morphology of the crystallites. The lattice parameters, obtained from a Rietveld refinement, are a = 8.7799(3) Å, b = 11.2248(4) Å and c = 5.2842(2) Å and a = 8.7757(3) Å, b = 11.2248(4) Å and c = 5.2831(2) Å for the precursor and LFZ, respectively. The reliability indices of the Rietveld analysis are χ^2 = 2.08, Bragg R-factor = 4.48 and RF-factor = 3.28 for the precursor and χ^2 = 2.64, Bragg R-factor = 4.67 and RF-factor=3.08 for LFZ. No significant difference between both kind of samples can be identified. Additionally, the parameters are in good agreement with the literature [6,15].
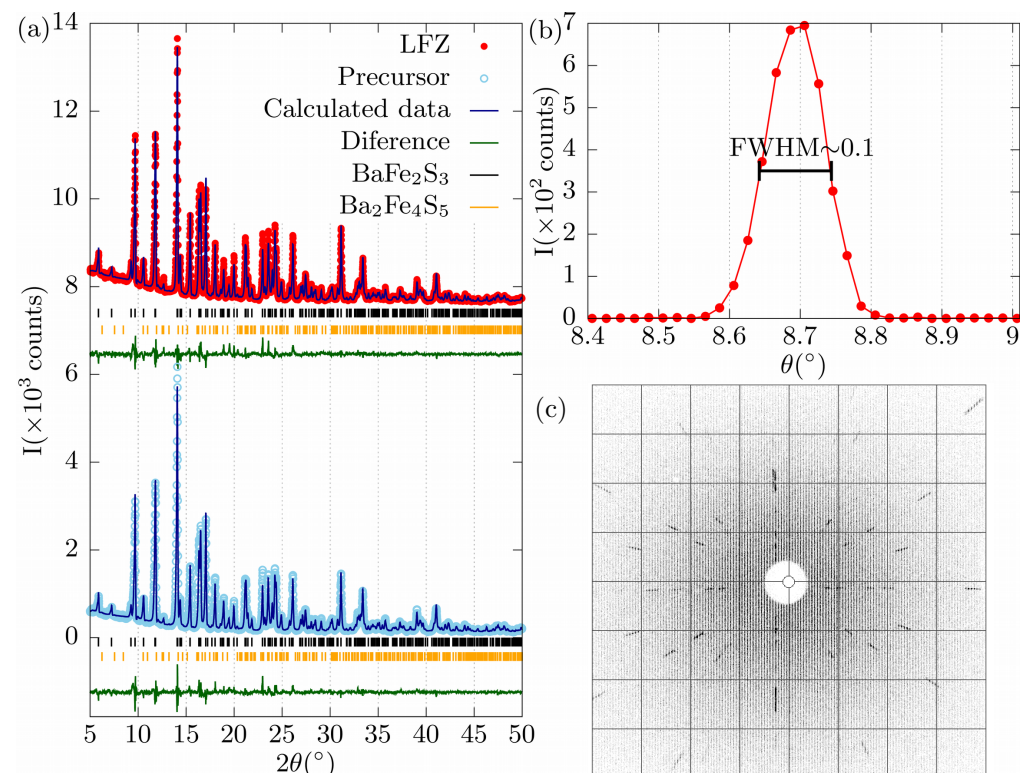

Figure 5. (**a**) Powder X-ray diffraction patterns and Rietveld refinements for precursor and LFZ samples. The data are shifted vertically for clarity. (**b**) Rocking curve of an LFZ-grown crystal for the (711) reflection. (**c**) Laue pattern for an LFZ-grown single crystal. The *c* direction (horizontal in the image) is ~10° away from the growth direction.

The analysis of the powder X-ray diffraction patterns indicates the presence of a small quantity of an impurity phase for both samples. Such extra reflections, often accompanying the 123 phase, have been proposed to correspond to $Ba_2Fe_4S_5$, which could be the average structure of a $BaFe_2S_3$ polymorph [30]. From the Rietveld refinement, the fraction of $Ba_2Fe_4S_5$ can be estimated to be ~2.1 wt % and ~2.6 wt % for the precursor and LFZ, respectively. The presence of an extra phase could be expected from the incongruent

melting of $BaFe_2S_3$ as observed from the penetration effect in the feed, which is also compatible with our preliminary DTA measurements.

The crystal structure of the LFZ crystal was also studied using single crystal X-ray diffraction. Experimental details on the data collection and results of the structural refinement are summarized in Table 2; the fractional atomic coordinates, equivalent isotropic displacement parameters, and occupation factors are compiled in Table 3; the anisotropic displacement parameters are listed in Table 4.

Table 2. Details on data collection and structure refinement of a LFZ crystal as determined from single crystal X-ray diffraction.

Crystal Data		Data Collection		Refinement	
Temperature (K)	295	$2\,\theta_{max}$ (°)	62.93	$N_{parameters}$	21
Space group	*Cmcm*	*Absorption correction*	Multiscan	$R_1 > 4\sigma$ (%)	1.46
a (Å)	8.7757(3)	T_{min}	0.5834	R_1 *all* (%)	1.86
b (Å)	11.2248(4)	T_{max}	0.7462	$wR_2 > 4\sigma$ (%)	3.13
c (Å)	5.2831(2)	$N_{measured}$	5807	wR_2 *all* (%)	3.25
Z	4	$N_{independent}$	499	*G.O.F*	1.140
M_r	345.17	R_{int} (%)	2.93	$\Delta\rho_{min}$ (e·A^{-3})	−0.865
ρ_{calc} (g·cm^{-3})	4.406			$\Delta\rho_{max}$ (e·A^{-3})	0.889
μ (mm^{-1})	14.009			*weight w (a,b)*	0.0160
					0.4559

T_{min} = minimum transmission, T_{max} = maximum transmission, $R_1 = \sum \| F_0 \| - \| F_c \| / \sum \| F_0 \|$, $wR_2 = \{\sum[w(F_0^2 - F_c^2)^2]/\sum[w(F_0^2)^2]\}^{1/2}$, $w = 1/[(\sigma^2(F_0^2)) + (aP)^2 + bP]$ where $P = [2F_c^2 + max(F_0^2, 0)]/3$.

Table 3. Fractional atomic coordinates, equivalent isotropic displacement parameters, and occupation factors of a LFZ single crystal at 295 K.

Atom	Site	x	y	z	U_{eq}(Å^2)	Occupancy
Ba	4c	0.5	0.18632(2)	0.25	0.01854(8)	1
Fe	8e	0.34635(4)	0.5	0	0.01115(9)	1.000(2)
S_1	4c	0.5	0.61569(8)	0.25	0.0115(2)	1
S_2	8g	0.20762(8)	0.37821(7)	0.25	0.0194(2)	1

Table 4. Anisotropic displacement parameters (Å^2) of a LFZ crystal at 295 K.

Atom	U_{11}	U_{22}	U_{33}	U_{23}	U_{13}	U_{12}
Ba	0.0187(1)	0.0231(1)	0.0138(1)	0	0	0
Fe	0.0098(2)	0.0162(2)	0.0074(2)	0.00003(14)	0	0
S_1	0.0118(3)	0.0133(4)	0.0093(4)	0	0	0
S_2	0.0188(3)	0.0280(3)	0.0113(3)	0	0	−0.0124(3)

In agreement with the results of the powder X-ray diffraction, the analysis of systematic extinctions and the subsequent structure refinement confirm that the LFZ sample crystallizes in the orthorhombic space group *Cmcm* (No. 63). Hirata et al. proposed that the presence of Fe vacancies affects the electronic and magnetic properties in $BaFe_2S_3$ [16]. In order to exclude this issue, the Fe-occupancy was allowed to vary freely during the crystal structure refinement. However, in line with the results from the EDX analysis, no compelling factor was found to suggest a Fe off-stoichiometry. The final refinement with the anisotropic atomic displacement parameters and consideration of possible Fe vacancies converged at final R_1(all data) = 1.86 % and wR_2(all data) = 3.25 %, showing a good agreement with previous reports [15].

X-ray diffraction experiments on single crystals show a full width at half maximum (FWHM) of ~0.1 ° for the rocking curve of the (711) reflection as presented in Figure 5b. A typical Laue backscattering image for a LFZ crystal is shown in Figure 5c. To obtain this image, the crystal was rotated, indicating that the growth direction is ~10° off the *c*-axis.

Figure 6a shows the temperature (T) dependence of the magnetization divided by the applied magnetic field (M/H) for crystals of the precursor and LFZ. A magnetic field of $\mu_0 H$ = 5 T along the c-axis was used. Below room temperature, the magnetization decreases with decreasing temperature opposing the typical Curie–Weiss behavior for three-dimensional localized magnets. This behavior is widely observed in this material [6,15,18,31] and is related to its low dimensional structure. Spin correlations within the ladders are present at temperatures well above T_N, the temperature at which long-range antiferromagnetic order sets in [32,33]. The kink in the magnetization at T_N indicates the transition to three-dimensional long-range antiferromagnetic order. The Néel temperature, defined as the minimum in the temperature derivative of the magnetization ($\mathrm{d}M/\mathrm{d}T|_{\min}$), is T_N = 109.5(6) K for the precursor and T_N = 119.8(6) K for the LFZ crystal as shown in Figure 6a. The higher T_N in the crystal grown by the laser-assisted floating zone method indicates an important improvement given that samples with lower T_N were reported to show no superconductivity under hydrostatic pressure [6].
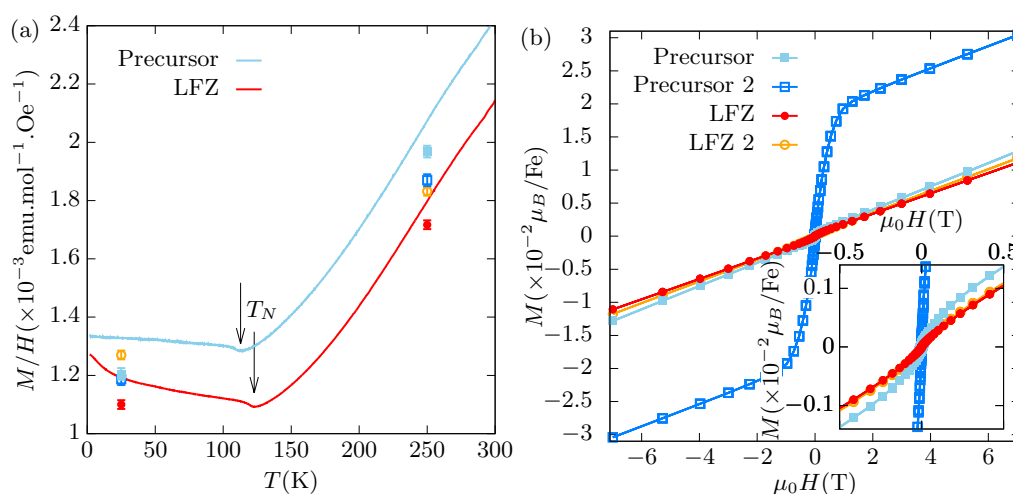

Figure 6. (**a**) Temperature dependence of the magnetization divided by the magnetic field for precursor and LFZ crystals measured with an applied magnetic field of $\mu_0 H$ = 5 T parallel to the c-axis. The dots show the slope of $M(H)$ for $\mu_0 H \geq 3$ T, the color and symbol indicate the sample as defined in (**b**). T_N indicates the Néel temperature defined as the minimum in the derivative, $\frac{\mathrm{d}M}{\mathrm{d}T}|_{\min}$. (**b**) Field dependence of the magnetization for two independent growths of both precursor and LFZ samples for T = 250 K. Inset: Low field region of M vs. H for the same samples of the main panel.

The higher absolute value of $M/H(T)$ in the precursor with respect to the LFZ sample in Figure 6a is commonly seen for crystals with ferromagnetic inclusions as presented in Ref. [15]. Further insight is provided by the field dependence of the magnetization shown in Figure 6b. We present data for two independent growths of the precursor and of the LFZ samples. A characteristic jump at low fields is observed for the precursor, which depends on the batch as well as on the sample. No hysteresis is seen for any of the LFZ samples as shown in the inset of Figure 6b. This jump could be related to the saturation of an extrinsic ferromagnetic contribution (less than 2 mol% if we assume it to be Fe). Such a small quantity of an impurity phase can pass unnoticed in a powder X-ray diffraction experiment, but it was occasionally observed in the compositional analysis. On the other hand, the jump is practically absent in crystals from two independent growths with the laser-assisted floating zone method. This reflects two important characteristics of the LFZ crystals: first, that ferromagnetic inclusions are successfully removed, yielding cleaner single crystals, and second, that this occurs in a reproducible way, in contrast to the standard procedure. The higher purity of the LFZ crystals of $BaFe_2S_3$ is also reflected in the lower absolute values of M/H, which are closer to the magnetic susceptibility at 25 K and 250 K obtained from the slope of $M(H)$ well above the jump (Honda–Owen analysis [34]), as shown in Figure 6a.

The normalized resistivity as a function of the inverse temperature for precursor and LFZ crystals is presented in Figure 7. Both samples exhibit an insulating behavior with two characteristic temperatures, T_N and T^*, which are indicated with arrows in the logarithmic derivative of the resistivity ($d\ln\rho/d(1/T)$). The Néel temperature is T_N = 110.1(5) K for the precursor and T_N = 121.0(4) K for the LFZ crystal, in good agreement with the values obtained from magnetization measurements. The temperature of the additional high-T anomaly in the resistivity is higher in the case of the precursor (T^* = 198(2) K) than in the case of the LFZ crystal (T^* = 176(2) K). The origin of T^* is still under debate, but it has been suggested to be related to orbital order [7,16].

The logarithmic derivative of the resistivity reveals a complex and different behavior for both samples. The LFZ crystal presents a region above $\sim$60 K and below $\sim$100 K consistent with a thermally activated behavior ($\rho=\rho_0 e^{\Delta/T}$) with a gap of Δ = 54(2) meV. This value is slightly higher than in previous reports [15,16]. On the other hand, in the same temperature region, the precursor presents a behavior compatible with a 1D variable range hopping ($\rho = \rho_0 e^{(T_0/T)^{1/2}}$) [35], also reported in the literature [15,16,18]. Another important difference is the region near the antiferromagnetic transition: while a sharp peak is observed in $d\ln\rho/d(1/T)$ for the LFZ crystal, the precursor presents a broad hump with a tiny peak at T_N. These features, together with the higher value of T_N in the LFZ samples, reflect the improvement in the quality of the samples grown by the laser-assisted floating zone method.
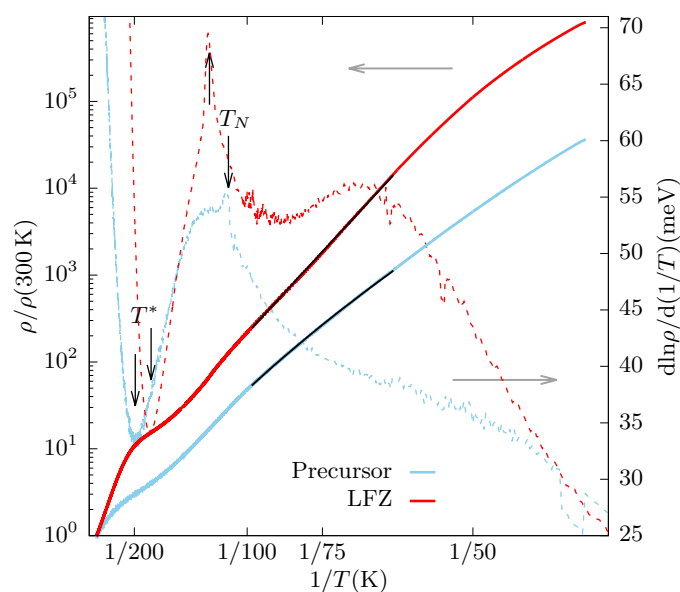

Figure 7. Normalized resistivity (left axis) and derivative of the logarithm of the resistivity (right axis) as a function of the inverse temperature for precursor and LFZ crystals. The Néel temperature and T^* are indicated with arrows in $d\ln\rho/d(1/T)$. The fitted thermally activated behavior for the LFZ crystal and the 1D variable range hopping for the precursor are presented as black continuous lines.

4. Conclusions

We show that the quality of $BaFe_2S_3$ crystals can be greatly improved when grown by a laser-assisted floating zone method compared to that of crystals grown using the method widely reported in the literature [6,15,16]. The success of the growth of high-quality $BaFe_2S_3$ crystals is due to specific characteristics of the laser-assisted floating zone furnace compared, for example, to a conventional image furnace equipped by halogen lamps. The laser-assisted FZ furnace presents a much steeper temperature gradient that strongly suppresses the penetration effect and allows to maintain a stable molten zone even in case of porous feed rods, which is useful for the growth of incongruently melting compounds.

While ferromagnetic impurity phases in variable amounts are ubiquitous in the precursor crystals and influence the magnetism and transport behavior observed in the samples,

such impurity phases are absent in laser-grown crystals. Therefore, the crystals grown by the laser-assisted floating zone method provide a more reliable insight into the intrinsic properties of $BaFe_2S_3$.

Data Availability Statement: The data are contained within the article.

Conflicts of Interest: The authors declare no conflict of interest. The funders had no role in the design of the study; in the collection, analyses, or interpretation of data; in the writing of the manuscript; or in the decision to publish the results.

References

1. Kamihara, Y.; Watanabe, T.; Hirano, M.; Hosono, H. Iron-based layered superconductor La[$O_{1-x}F_x$]FeAs (x = 0.05 − 0.12) with T_c = 26 K. *J. Am. Chem. Soc.* **2008**, *130*, 3296–3297. [CrossRef] [PubMed]
2. Fernandes, R.; Chubukov, A.; Schmalian, J. What drives nematic order in iron-based superconductors? *Nat. Phys.* **2014**, *10*, 97–104. [CrossRef]
3. Hosono, H.; Kuroki, K. Iron-based superconductors: Current status of materials and pairing mechanism. *Phys. C Supercond. Appl.* **2015**, *514*, 399–422. [CrossRef]
4. Hao, N.; Hu, J. Topological quantum states of matter in iron-based superconductors: from concept to material realization. *Natl. Sci. Rev.* **2019**, *6*, 213–226. [CrossRef]
5. Aswathy, P.; Anooja, J.; Sarun, P.; Syamaprasad, U. An overview on iron based superconductors. *Supercond. Sci. Technol.* **2010**, *23*, 073001. [CrossRef]
6. Takahashi, H.; Sugimoto, A.; Nambu, Y.; Yamauchi, T.; Hirata, Y.; Kawakami, T.; Avdeev, M.; Matsubayashi, K.; Du, F.; Kawashima, C.; et al. Pressure-induced superconductivity in the iron-based ladder material $BaFe_2S_3$. *Nat. Mater.* **2015**, *14*, 1008. [CrossRef]
7. Yamauchi, T.; Hirata, Y.; Ueda, Y.; Ohgushi, K. Pressure-Induced Mott Transition Followed by a 24-K Superconducting Phase in $BaFe_2S_3$. *Phys. Rev. Lett.* **2015**, *115*, 246402. [CrossRef]
8. Ying, J.; Lei, H.; Petrovic, C.; Xiao, Y.; Struzhkin, V.V. Interplay of magnetism and superconductivity in the compressed Fe-ladder compound $BaFe_2Se_3$. *Phys. Rev. B* **2017**, *95*, 241109. [CrossRef]
9. Svitlyk, V.; Garbarino, G.; Rosa, A.; Pomjakushina, E.; Krzton-Maziopa, A.; Conder, K.; Nunez-Regueiro, M.; Mezouar, M. High-pressure polymorphism of $BaFe_2Se_3$. *J. Phys. Condens. Matter* **2019**, *31*, 085401. [CrossRef]
10. Craco, L.; Leoni, S. Microscopic description of localization-delocalization transitions in $BaFe_2S_3$. *Phys. Rev. B* **2018**, *98*, 195107. [CrossRef]
11. Roh, S.; Shin, S.; Jang, J.; Lee, S.; Lee, M.; Seo, Y.S.; Li, W.; Biesner, T.; Dressel, M.; Rhee, J.Y.; et al. Magnetic-order-driven metal-insulator transitions in the quasi-one-dimensional spin-ladder compounds $BaFe_2S_3$ and $BaFe_2Se_3$. *Phys. Rev. B* **2020**, *101*, 115118. [CrossRef]

12.	Pizarro, J.M.; Bascones, E. Strong electronic correlations and Fermi surface reconstruction in the quasi-one-dimensional iron superconductor $BaFe_2S_3$. *Phys. Rev. Mater.* **2019**, *3*, 014801. [CrossRef]

13.	Zhang, Y.; Lin, L.; Zhang, J.J.; Dagotto, E.; Dong, S. Pressure-driven phase transition from antiferromagnetic semiconductor to nonmagnetic metal in the two-leg ladders AFe_2X_3 ($A =$ Ba, K; $X =$ S, Se). *Phys. Rev. B* **2017**, *95*, 115154. [CrossRef]

14.	Materne, P.; Bi, W.; Zhao, J.; Hu, M.Y.; Amigó, M.L.; Seiro, S.; Aswartham, S.; Büchner, B.; Alp, E.E. Bandwidth controlled insulator-metal transition in $BaFe_2S_3$: A Mössbauer study under pressure. *Phys. Rev. B* **2019**, *99*, 020505. [CrossRef]

15.	Amigó, M.L.; Stahl, Q.; Maljuk, A.; Wolter, A.U.B.; Hess, C.; Geck, J.; Wurmehl, S.; Seiro, S.; Büchner, B. The role of the nominal iron content in the structural, compositional and physical properties of $BaFe_{2+\delta}S_3$. *arXiv* **2021**, arXiv:2101.07823.

16.	Hirata, Y.; Maki, S.; Yamaura, J.i.; Yamauchi, T.; Ohgushi, K. Effects of stoichiometry and substitution in quasi-one-dimensional iron chalcogenide $BaFe_2S_3$. *Phys. Rev. B* **2015**, *92*, 205109. [CrossRef]

17.	Sun, H.; Li, X.; Zhou, Y.; Yu, J.; Frandsen, B.A.; Wu, S.; Xu, Z.; Jiang, S.; Huang, Q.; Bourret-Courchesne, E.; et al. Nonsuperconducting electronic ground state in pressurized $BaFe_2S_3$ and $BaFe_2S_{2.5}Se_{0.5}$. *Phys. Rev. B* **2020**, *101*, 205129. [CrossRef]

18.	Zhang, X.; Zhang, H.; Ma, Y.; Wang, L.; Chu, J.; Hu, T.; Mu, G.; Lu, Y.; Cai, C.; Huang, F.; et al. In situ annealing effects on magnetic properties and variable-range hopping of iron-based ladder material $BaFe_2S_3$. *Sci. China Phys. Mech. Astron.* **2018**, *61*, 77421. [CrossRef]

19.	Telang, P.; Maljuk, A.; Rout, D.; Hu, R.; Skoulatos, M.; Karmakar, K.; Seiro, S.; Roessli, B.; Stuhr, U.; Büchner, B.; et al. Laser-diode-heated floating-zone crystal growth of $ErVO_3$. *J. Cryst. Growth* **2019**, *507*, 406–412. [CrossRef]

20.	Rodríguez-Carvajal, J. Recent advances in magnetic structure determination by neutron powder diffraction. *Phys. B Condens. Matter* **1993**, *192*, 55–69. [CrossRef]

21.	*Bruker, APEX3 v2018.1-0*; Bruker AXS Inc.: Madison, WI, USA, 2017.

22.	*SAINT(V8.30A)*; Bruker AXS Inc.: Madison, WI, USA, 2017.

23.	Krause, L.; Herbst-Irmer, R.; Sheldrick, G.M.; Stalke, D. Comparison of silver and molybdenum microfocus X-ray sources for single-crystal structure determination. *J. Appl. Crystallogr.* **2015**, *48*, 3–10. [CrossRef]

24.	Sheldrick, G.M. A short history of SHELX. *Acta Crystallogr. Sect. A Found. Crystallogr.* **2008**, *64*, 112–122. [CrossRef] [PubMed]

25.	Farrugia, L.J. WinGX suite for small-molecule single-crystal crystallography. *J. Appl. Crystallogr.* **1999**, *32*, 837–838. [CrossRef]

26.	Seiro, S.; Deppe, M.; Jeevan, H.; Burkhardt, U.; Geibel, C. Flux crystal growth of $CeCu_2Si_2$: Revealing the effect of composition. *Phys. Status Solidi* **2010**, *247*, 614–616. [CrossRef]

27.	Goldstein, J.; Newbury, D.E.; Joy, D.C.; Lyman, C.E.; Echlin, P.; Lifshin, E.; Sawyer, L.; Michael, J.R. *Scanning Electron Microscopy and X-ray Microanalysis*; Springer: Berlin/Heidelberg, Germany, 2003.

28.	Hong, H.; Steinfink, H. The crystal chemistry of phases in the Ba-Fe-S and Se systems. *J. Solid State Chem.* **1972**, *5*, 93–104. [CrossRef]

29.	Iglesias, J.; Steinfink, H. Triangular prismatic coordination in ternary chalcogenides. *Z. Für Krist.-Cryst. Mater.* **1975**, *142*, 398–408. [CrossRef]

30.	Swinnea, J.S.; Eisman, G.; Perng, T.; Kimizuka, N.; Steinfink, H. The crystal structure of "$Ba_2Fe_4S_5$": A two-dimensional array of FeS_4 tetrahedra. *J. Solid State Chem.* **1982**, *41*, 104–108. [CrossRef]

31.	Du, F.; Ueda, Y.; Ohgushi, K. Large Magnon Contributions to Thermal Conductance in Quasi-One-Dimensional Fe-Based Ladder Compounds $BaFe_2(S_{1-x}Se_x)_3$. *Phys. Rev. Lett.* **2019**, *123*, 086601. [CrossRef]

32.	Johnston, D. Antiferromagnetic exchange in two-leg spin-1/2 ladders. *Phys. Rev. B* **1996**, *54*, 13009. [CrossRef] [PubMed]

33.	Tiwary, S.K.; Vasudevan, S. Single crystal magnetic susceptibility of the quasi-one-dimensional antiferromagnet $KFeS_2$. *Solid State Commun.* **1997**, *101*, 449–452. [CrossRef]

34.	Bates, L.F. *Modern Magnetism*; Cambrige at University Press: Cambrige, UK, 1948.

35.	Fogler, M.M.; Teber, S.; Shklovskii, B.I. Variable-range hopping in quasi-one-dimensional electron crystals. *Phys. Rev. B* **2004**, *69*, 035413. [CrossRef]